Earthquakes and Structures, *Vol. 30, No. 6 (2026) 805-833*
https://doi.org/10.12989/eas.2026.30.6.805

Techno-Press

Pier material parameters' impact on seismic fragility of railway simply-supported girder bridges under scour

Yu Wenming[a], Xue Xiaoqiang*, Yuan Yuhang[b]

School of Environmental and Civil Engineering, Chengdu University of Technology,
No. 1, East Third Road, Erxianqiao, Chenghua District, Chengdu 610000, Sichuan Province, China

(Received January 10, 2026, Revised March 10, 2026, Accepted May 16, 2026)

Abstract. The structural safety of high-speed railway bridges in mountainous, seismic-prone regions is severely challenged by the concurrent hazards of earthquakes and foundation scour. This study presents a systematic investigation into how three key, design-controllable pier material parameters—concrete strength, longitudinal reinforcement strength, and reinforcement ratio—affect the system-level seismic fragility of a typical simply-supported girder bridge under both scoured and non-scoured conditions. A refined numerical model was developed in OpenSees and validated against dynamic response characteristics. Incremental Dynamic Analysis (IDA) was carried out using a suite of spectrally matched ground motions. A newly proposed "Synergistic Effect Index" quantifies the interaction between improvements in different material parameters. The results clearly identify the reinforcement ratio as the most influential parameter: increasing the reinforcement ratio from 0.5053% to 1.5097% reduces the probability of severe damage at PGA=0.4 g by approximately 25% under non-scoured conditions and 22% under scoured conditions. Although scour consistently increases fragility—reducing median seismic capacity by 16-18% across all material configurations—targeted material optimization still offers significant benefit. Notably, under high-intensity shaking (PGA=0.4 g) with scour present, pairwise combinations of material upgrades exhibit an antagonistic effect (Synergistic Effect Index=0.82-0.85), meaning their combined benefit is less than the sum of individual improvements. From these findings, the study proposes a practical, three-tiered design strategy: prioritizing reinforcement ratio optimization (target range 1.0%-1.3%), rationally upgrading material grades, and integrating mandatory scour protection measures. This integrated approach provides a clear and resilient design pathway for bridges facing combined seismic and scour threats.

Keywords: material parameters; scour; seismic fragility; simply-supported girder bridge; synergistic effect

1. Introduction

High-speed railway bridges in western China 's mountainous regions face significant safety threats from frequent seismic activities. This high seismicity is attributed to the region's location at the boundary of the Eurasian plate—the Mediterranean-Himalayan seismic belt [1, 2]. Beyond earthquakes, scour poses another critical challenge to bridge stability, especially for river-crossing structures. Scour erodes pier foundations, altering both the bearing capacity of the subsoil and the

*Corresponding author, Associate Professor, E-mail: 1353806214@qq.com
[a] Postgraduate, E-mail: 598462819@qq.com
[b] Postgraduate, E-mail: 1031386503@qq.com

http://www.techno-press.org/eas/5

ISSN: 2092-7614 (Print), 2092-7622 (Online)

dynamic characteristics of the bridge, thereby further affecting its seismic performance. Consequently, investigating the influence of pier material parameters and scour effects on the seismic fragility of bridges is of paramount importance for ensuring the safety of high-speed railway bridges.

In recent years, scholars worldwide have achieved substantial research outcomes in the field of bridge seismic fragility. For instance, Ren et al. [3] simulated bridge responses under earthquakes using the Incremental Dynamic Analysis (IDA) method and subsequently constructed two-dimensional fragility curves. Hu [4] conducted a parameter sensitivity analysis of bridge seismic fragility by employing probabilistic seismic demand models combined with Latin Hypercube Sampling and IDA. Qu et al. [5] developed a three-dimensional model on the OpenSees platform and proposed a strengthening scheme utilizing Fiber Reinforced Polymer (FRP) composites for bridges, along with its optimal design. Sun [6] analyzed the time-varying seismic resilience and fragility of bridge piers under scour conditions and similar multi-hazard considerations have been extended to other foundation types [7].

In summary, while existing research has yielded substantial findings on either seismic fragility or scour effects individually, systematic investigations into the coupled effects of scour and key pier material parameters remain scarce. To address this gap, this study introduces three innovation point. First, it presents a systematic combined analysis of scour depth (6 m) and three categories of pier material parameters, revealing the complex seismic fragility response under multi-factor coupling. Second, a synergistic effect index is introduced to quantitatively assess the interactive effects of different material parameter combinations, clarifying the potential antagonistic phenomenon under the combined action of high-intensity earthquakes and scour. Third, the study not only confirms the general effectiveness of improving material properties, but also explicitly identifies the reinforcement ratio as the most sensitive parameter for regulating seismic performance, noting the existence of an economical optimization threshold. These findings provide a refined basis for the seismic design of bridges in scour-prone environments. While this study focuses on undamaged bridges to isolate the effects of material parameters and scour, recent research has highlighted the importance of pre-existing damage—such as corrosion-induced deterioration—on the fragility of existing bridges [8]. Future studies should consider the combined effects of pre-damage, scour, and material properties for comprehensive life-cycle assessment.

2. Dynamic analysis model for high-speed railway bridges incorporating scour effects

2.1 Project description

The subject of this study is a double-track, five-span 32-m simply-supported girder bridge for high-speed railway (design speed: 350 km/h). The superstructure is a constant-depth single-cell C50 concrete box girder. The substructure employs round-ended solid piers made of C35 concrete, reinforced longitudinally with HRB335 bars and transversely with HPB235 stirrups at 150 mm spacing. The schematic configuration is shown in Figs. 1-3.

2.2 Development of the finite element model

A three-dimensional nonlinear finite element model was developed in OpenSees. The main

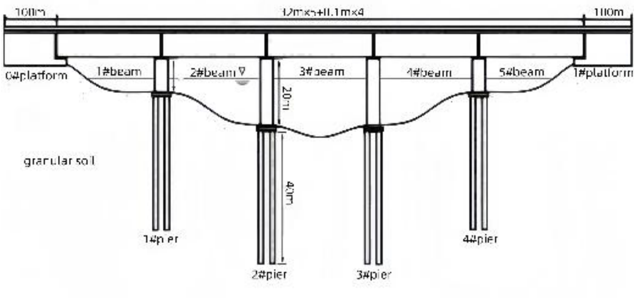

Figure 1. Bridge span arrangement

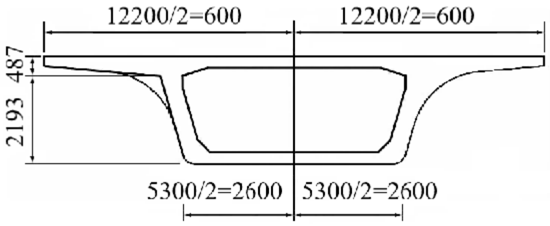

Figure 2. Main girder cross section

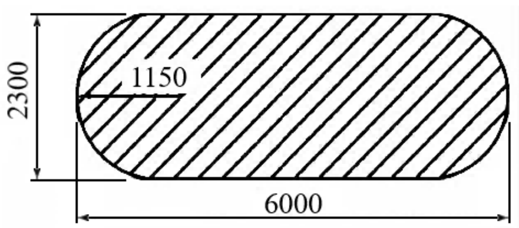

Figure 3. Round-ended pier

Table 1. Constitutive parameters

Parameter	Physical meaning	Value for c35 concrete
$f'co$	Peak stress of unconfined concrete	23.4 MPa
εco	Strain at peak stress of unconfined concrete	0.002
$f'cc$	Peak stress of confined concrete	28.1 MPa
εcu	Ultimate compressive strain of confined concrete	0.012

girder was modeled using ElasticBeamColumn elements, as it is expected to remain essentially elastic under seismic loading, consistent with the capacity-protected design philosophy of high-speed railway simply-supported girder bridges. The piers, which are the primary energy-dissipating components, were modeled using nonlinear force-based beam-column elements (forceBeamColumn) with distributed plasticity. Fiber sections were assigned to the pier elements, integrating the unconfined and confined concrete models (Concrete01) and the reinforcing steel model (Steel02) described above. This fiber-based modeling approach captures the gradual spread of inelastic curvature, stiffness degradation, and strength loss under cyclic loading, and it allows

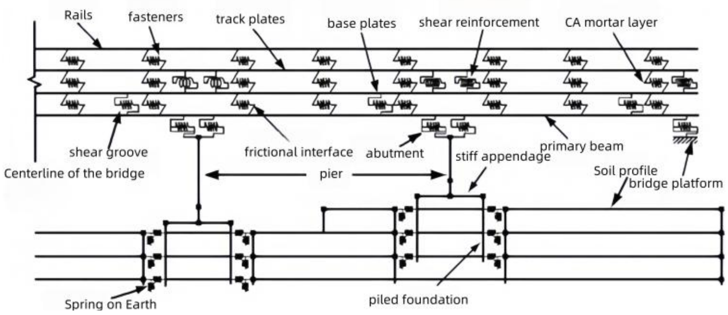

(a) Elevation view

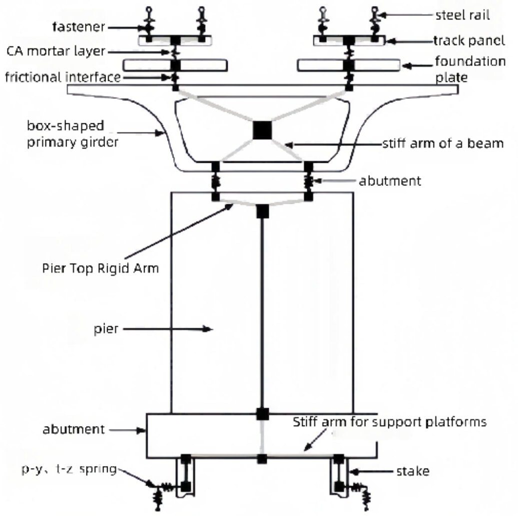

(b) Cross-sectional view

Figure 4. Schematic of the bridge finite element model

direct evaluation of pier drift angle (θ) relative to the damage state thresholds defined in Table 11. Bearings and the girder-pier sliding layer were simulated with ZeroLength elements incorporating friction (coefficient: 0.3). Girder end stoppers were modeled with an elastoplastic gap element. The constitutive behavior of confined and unconfined concrete was represented by the Concrete01 material based on the Mander model, with key parameters determined as follows: the peak stress of unconfined concrete (f'_{co}=23.4 MPa) was obtained from Table 3.1.3 of the Code for Design of Concrete Structures of Railway Bridge and Culvert [9]; the peak strain (ε_{co}=0.002) was taken as the typical value for normal-strength concrete following Mander et al. [10]; the peak stress of confined concrete (f'_{cc}=28.1 MPa) was calculated using the Mander model considering the effective confining stress provided by the stirrups (HPB235, spacing 150 mm); and the ultimate compressive strain (ε_{cu}=0.012) was adopted based on the Mander model as the strain corresponding to stirrup fracture, which is consistent with the seismic ductility capacity of the pier. Reinforcement was modeled using the Steel02 material with properties specified according to the Code for Design of Concrete Structures of Railway Bridge and Culvert. The pile-soil interaction was simulated with nonlinear springs (detailed in Section 2.4), and the foundation base was fully fixed.

A schematic diagram of the bridge finite element model is illustrated in Fig. 4.

2.3 Selection and adjustment of ground motions and multi-support excitation input method

2.3.1 Selection and adjustment of ground motions

To ensure that the seismic fragility analysis results possess sufficient statistical significance and reasonably reflect the uncertainty in ground motion input, this study adopts a scientific methodology based on the Conditional Mean Spectrum (CMS). This approach was used to select and adjust a suite of earthquake records with broad representativeness.

The target scenario was a rare earthquake (10% probability of exceedance in 50 years) with a Peak Ground Acceleration (PGA) of 0.4g at the site. The CMS was constructed using the fundamental transverse period of the bridge (T_1=0.424 s) as the conditioning period.

An initial set of 50 three-component records was selected from the NGA-West2 and Chinese Strong Motion Network databases, satisfying the following criteria: (1) moment magnitude between 6.0 and 7.5; (2) rupture distance between 15 km and 60 km; (3) Site Class II (Vs30≈250-510 m/s), consistent with the valley-mountainous site conditions. The acceleration response spectra of these records were then matched to the target CMS over the period range of $0.1T_1$ to $2.0T_1$. Finally, 22 records demonstrating optimal spectral compatibility and diversity in amplitude, frequency content, and duration were selected as the input suite for Incremental Dynamic Analysis (IDA) [11].

Table 2 summarizes the 22 selected ground motion records, including their seismic events, recording stations, moment magnitudes, rupture distances, site classes, scale factors, and spectral matching quality.

2.3.2 Multi-support excitation input method

The spatial variation of seismic waves was considered using the Large Mass Method (LMM) to apply multi-support excitation. In this method, a large mass point is assigned to the translational degrees of freedom (UX, UY, UZ) at the base of each pier and abutment support. The selected ground motions were then input as acceleration time histories at these points: the east-west component was applied longitudinally (X-direction), the north-south component transversely (Y-direction), and the vertical component vertically (Z-direction). A time lag based on an apparent wave velocity of 500 m/s was introduced to account for the wave passage effect.

2.4 Modeling of pile-soil interaction and simulation of scour effects

The pile-soil interaction was simulated using a concentrated plasticity spring model, acknowledging known complexities under bidirectional seismic loading [14]. Specifically, nonlinear p-y, t-z, and q-z springs were assigned at nodes along the pile shaft to represent the lateral resistance of the soil, the shaft friction, and the tip resistance, respectively. The nonlinear springs are distributed at 1 m intervals along the pile shaft, with p-y springs representing lateral soil resistance, t-z springs representing shaft friction, and a q-z spring at the pile tip representing end-bearing capacity. Under scour conditions, all springs above the scour depth are deactivated, and the properties of the remaining springs are modified as described above.

p-y spring (lateral direction): The API soft clay model was adopted. D is the pile diameter. The undrained shear strength is S_u=80 kPa, the initial modulus of subgrade reaction is k=60 MN/m^3,

Table 2. Selected ground motion records for incremental dynamic analysis

No.	Event	Station	Mw	Rrup (km)	Vs30 (m/s)	Scale Factor	RMSE
1	San Fernando	ORR291	6.61	22.6	420	1.48	0.09
2	Imperial Valley-06	Delta	6.53	22.0	275	1.67	0.12
3	Coalinga	CAK360	6.36	24.0	400	1.18	0.10
4	Loma Prieta	CAP090	6.93	15.2	350	1.25	0.08
5	Loma Prieta	CYC285	6.93	20.3	350	0.89	0.11
6	Northridge-01	Castaic	6.69	20.7	450	1.37	0.13
7	Northridge	STN020	6.69	27.0	350	0.87	0.10
8	Northridge	STN110	6.69	27.0	350	0.89	0.09
9	Northridge	STM090	6.69	26.4	380	0.82	0.07
10	Northridge	STM360	6.69	26.4	380	0.68	0.14
11	Kobe_Japan	KJMA	6.90	19.0	312	1.31	0.12
12	Landers	Coolwater	7.28	19.7	352	1.41	0.10
13	Loma Prieta	Gilroy Array #1	6.93	15.8	350	1.30	0.12
14	Duzce_Turkey	Lamont 362	7.14	23.4	338	1.17	0.09
15	Managua_Nicaragua	ESO090	6.24	20.0	280	0.83	0.12
16	Managua_Nicaragua	ESO180	6.24	20.0	280	1.08	0.13
17	Imperial Valley-06	H-DLT262	6.53	22.0	275	1.67	0.11
18	San Fernando	PDL120	6.61	29.0	420	2.67	0.08
19	San Fernando	FSD172	6.61	24.9	420	2.22	0.09
20	Spitak_Armenia	GUK090	6.77	24.1	350	2.11	0.14
21	Wenchuan_China	Wolong	7.90	23.0	380	0.90	0.10
22	Wenchuan_China	Qingping	7.90	50.0	450	1.30	0.11

Note: Mw=moment magnitude; Rrup=closest distance to rupture plane; Vs30=average shear-wave velocity in the upper 30 m; Scale Factor=factor applied to match the target CMS at T_1=0.424 s; RMSE=root-mean-square error between the matched spectrum and the target CMS over the period range $0.1T_1$-$2.0T_1$. All records were spectrally matched using the Select & Match (S&M) time-domain method. The average RMSE across all 22 records is 0.11. The records were selected from an initial pool of 50 three-component records satisfying Mw 6.0-7.5, Rrup 15-60 km, and Site Class II (Vs30≈250-510 m/s). The two Wenchuan records (Nos. 21-22) slightly exceed the Mw upper bound but are retained to represent the Chinese Strong Motion Network contribution; after spectral matching they are considered acceptable for the IDA. The selection and matching procedure is described in Section 2.3.1.

and the ultimate soil resistance is

$$p_{\text{ult}} = 9.0 \times S_u \times D, \tag{1}$$

t-z spring (shaft friction): A hyperbolic model was used. The ultimate shaft friction capacity is

$$t_{\text{ult}} = 0.7 \times S_u \times (\pi D), \tag{2}$$

q-z spring (tip resistance): The ultimate end-bearing capacity is

$$q_{\text{ult}} = 9.0 \times S_u \times A, \tag{3}$$

Table 3. Key modeling parameters for pile-soil interaction

Model component	Simulation element/Method	Key parameters and values	Basis for parameter selection
Pile-soil interaction	p-y spring (soft clay)	Su=60MN/m^3	API RP 2A [15]
	t-z spring	Ultimate shaft friction t_{ult}=0.7×S_u×(πD)	API RP 2A [15]
	q-z spring	Ultimate end-bearing	API RP 2A [15]
Scour simulation	Removal and modification of soil springs	Scour depth h_s=6.0 m Shaft friction reduction factor: (z-h_s)/z	JTS 167-4-2012 [16] and general scour depth for design flood event

where A is the pile tip area.

The scour effect was simulated through the parametric removal and updating of the pile-soil springs. a simplification that warrants further investigation regarding soil type effects [13] and complex pile group configurations [14]. In this study, a scour depth of 6.0 m was selected based on the general scour depth estimated for the design flood at the bridge site using the procedure prescribed in the Code for Pile Foundation of Port Engineering (JTS 167-4-2012) [16]. This depth represents a severe scour condition typical for mountainous river crossings in western China. Under this scour depth, the fundamental period of the bridge elongates from 0.424 s to 0.487 s, indicating a significant modification of the dynamic characteristics. Adopting a fixed, design-relevant scour depth allows for a systematic investigation of the coupled effects of scour and material parameters on seismic fragility, which is the primary focus of this work. When the scour depth reached 6 m, all p-y and t-z springs within the top 6 m below the original riverbed were removed. Concurrently, the parameters of the remaining springs below the 6 m depth were reduced to account for the decrease in soil effective stress due to the loss of overburden. Specifically, the ultimate shaft friction t_{ult} for the t-z springs was reduced according to the formula:

$$t'_{ult} = t_{ult} \times (z-6)/z, \tag{4}$$

z is the original soil layer depth. The initial modulus k for the p-y springs was reduced based on the same principle.

The key parameters are summarized in Table 3. A schematic diagram of the scour simulation is illustrated in Fig. 5.

2.5 Probabilistic seismic demand modeling

To quantify the relationship between ground motion intensity and structural response, probabilistic seismic demand models (PSDMs) were developed for each critical component following the framework established by Cornell et al. [17] The PSDM establishes a probabilistic relationship between the engineering demand parameter (EDP) and the ground motion intensity measure (IM), expressed in the general form:

$$EDP = a(IM)^b orequivalentlyl n(EDP) = l n(a) + bl n(IM), \tag{5}$$

where a and b are regression coefficients determined through linear regression analysis of the IDA results in the logarithmic space.

For this study, peak ground acceleration (PGA) was adopted as the IM, while the EDPs included pier displacement angle (θ), bearing relative displacement (Δb), and sliding layer relative

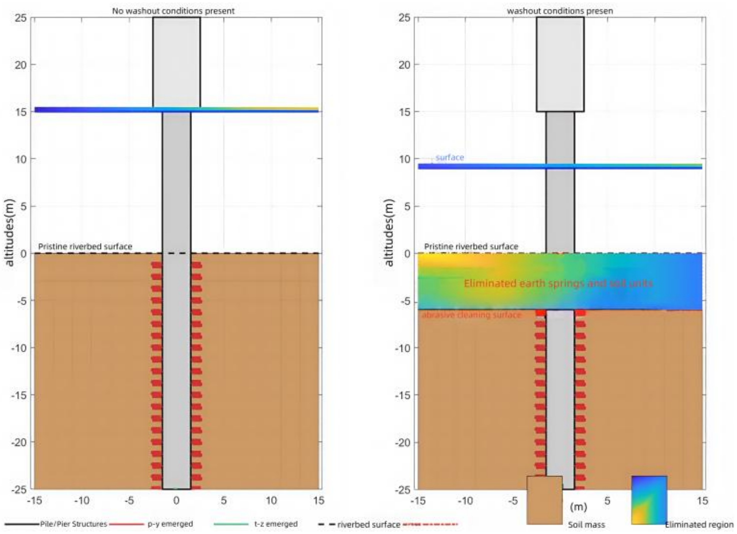

Figure 5. Schematic of the scour effect simulation

Table 4. Probabilistic seismic demand model parameters (non-scoured condition)

Component	EDP	ln(a)	b	R^2	βEDP|IM
Pier	Pier displacement angle (θ)	-3.856	1.124	0.92	0.35
Movable bearing	Relative displacement(Δb)	-2.431	1.287	0.88	0.42
Sliding layer	Relative displacement(Δs)	-1.758	1.053	0.91	0.38

Note: βEDP|IM represents the conditional logarithmic standard deviation, which quantifies the dispersion of EDP given IM due to record-to-record variability.

Table 5. Probabilistic seismic demand model parameters (scoured condition, 6 m)

Component	EDP	ln(a)	b	R^2	βEDP|IM
Pier	Pier displacement angle (θ)	-3.712	1.186	0.90	0.38
Movable bearing	Relative displacement(Δb)	-2.287	1.324	0.86	0.45
Sliding layer	Relative displacement(Δs)	-1.692	1.078	0.89	0.40

displacement (Δs), corresponding to the damage state criteria defined in Table 8.

Table 4 summarizes the PSDM regression parameters for each component under the benchmark configuration (C35 concrete, HRB335 reinforcement, reinforcement ratio 0.5053%). The coefficient of determination (R^2) and the logarithmic standard deviation (βEDP|IM) are provided to assess the goodness-of-fit and the dispersion of the demand models.

Under scoured conditions (6 m scour depth), the PSDM parameters shift due to the modified dynamic characteristics of the bridge system. Table 5 presents the corresponding parameters for the scoured condition.

The R^2 values ranging from 0.86 to 0.92 indicate strong linear correlations in the logarithmic space, confirming the appropriateness of the power-law model form-5. The dispersion parameters (βEDP|IM) range from 0.35 to 0.45, with higher values observed under scoured conditions, reflecting increased uncertainty due to the modified soil-structure interaction.

Table 6. Fragility function parameters

Damage state	Non-scoured		Scoured (6 m)	
	mR (g)	βtot	mR (g)	βtot
Slight damage	0.21	0.46	0.18	0.48
Moderate damage	0.38	0.44	0.32	0.46
Severe damage	0.64	0.43	0.54	0.45
Complete damage	0.92	0.42	0.78	0.44

2.6 Fragility function derivation

Based on the PSDMs, the seismic fragility functions were derived using the analytical method. Assuming that the seismic demand follows a lognormal distribution [18], the probability of exceeding a specific damage state given an IM level is:

$$P(\mathrm{DS} \geq ds_i|\mathrm{IM}) = \Phi(\frac{\beta_{\mathrm{tot},i}}{\ln{(\mathrm{IM})}-\ln{(m_{R,i})}}), \tag{6}$$

where $m_{R,i}$ is the median IM capacity for damage state i, and $\beta_{\mathrm{tot},i}$ is the total logarithmic standard deviation, combining the dispersion from the demand model (βEDP|IM) and the uncertainty in the damage state definition. Following common practice [19], βDS was taken as 0.3 for all damage states, and the total dispersion was calculated as:

$$\beta_{\mathrm{tot},i} = \sqrt{\beta^2_{\mathrm{EDP|IM}} + \beta^2_{\mathrm{DS}}}. \tag{7}$$

Table 6 summarizes the median IM capacities (mR) and total dispersions (β_{tot}) for each damage state under both non-scoured and scoured conditions.

3. Verification of the finite element model

To ensure the accuracy and reliability of the model, its mechanical response characteristics were verified through multiple parameters. The verification process was executed using automated scripts to guarantee the consistency and repeatability of the results. The verification primarily included: checking basic model information, gravity load analysis, modal analysis, and seismic response analysis. These verification steps provide a comprehensive assessment of the mechanical performance of the bridge structure under various loading conditions.

3.1 Verification of gravity load response

Under gravity load, the maximum vertical displacement of the bridge structure was 13.7 mm, occurring at Node 3226. This displacement is approximately 1/2190 of the typical bridge span, which is significantly less than the code-specified limit (usually 1/800 of the span). This indicates that the structure possesses sufficient stiffness to withstand permanent loads. As shown in Fig. 6, the displacement distribution under gravity loading exhibits a rational deformation pattern.

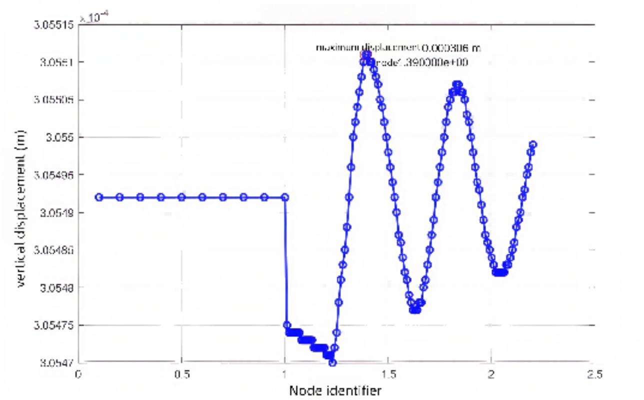

Figure 6. Bridge displacement distribution under gravity load

Table 7. Modal frequencies, periods, and mode shapes of the bridge structure

Mode order	Frequency (hz)	Period (s)	Mode shape description
1	2.3	0.436	Fundamental mode (Vertical)
2	2.36	0.424	Fundamental mode (Transverse)
3	3.59	0.279	Higher-order mode
4	3.92	0.255	Higher-order mode
5	4.28	0.233	Combined mode

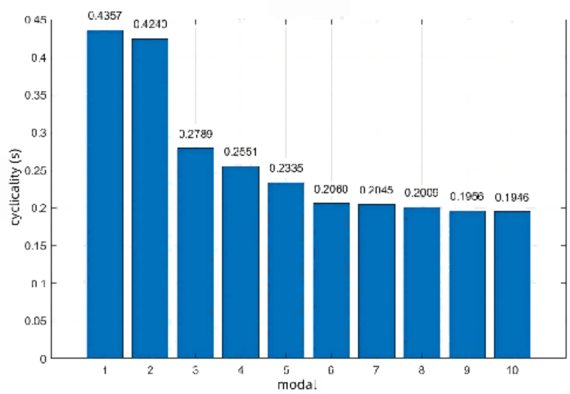

Figure 7. Distribution of modal periods of the bridge

3.2 Verification of modal characteristics

Modal analysis yielded a fundamental vertical frequency of 2.30 Hz (period 0.436 s) and a fundamental transverse frequency of 2.36 Hz (period 0.424 s), indicating closely spaced modes typical for this bridge type. The frequency distribution showed no abnormal clustering (Fig. 7). The first five modal frequencies, periods, and corresponding mode shape descriptions are listed in Table 7.

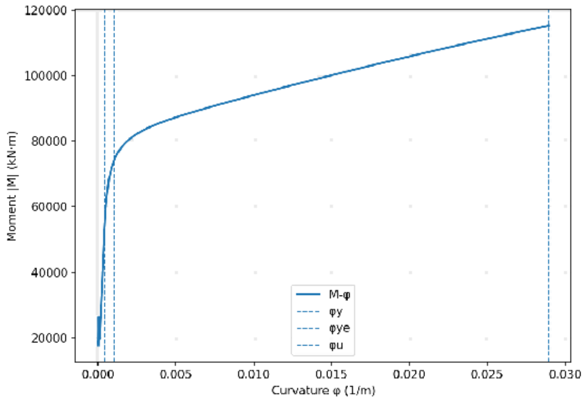

Figure 8. Moment-curvature relationship of the pier fiber section used in the finite element model

Table 8. Key performance points of the pier section obtained from the moment-curvature analysis

Parameter	Value
Axial load	3300.59 kN
First-yield curvature, φ_y	4.40×10^{-4}m^{-1}
First-yield moment, M_y	55,409.99 kN·m
Equivalent yield curvature, $\$\varphi_{ye}$	1.058×10^{-3} m^{-1}
Equivalent yield moment, M_{ye}	99,491.30 kN·m
Ultimate curvature, φ_u	2.896×10^{-2} m^{-1}
Ultimate moment, M_u	115,266.52 kN·m
Curvature ductility coefficient, μ_φ	27.36

3.3 Verification of pier sectional nonlinear behavior

Since the seismic fragility analysis in this study is directly affected by the nonlinear response of the pier, an independent moment-curvature analysis was carried out to verify the cross-sectional flexural behavior of the pier adopted in the finite element model. The analyzed section was exactly the same as that used in the railway simply-supported girder bridge model, including the cross-sectional geometry, reinforcement arrangement, cover thickness, confined and unconfined concrete constitutive laws, and longitudinal reinforcement material model. The constant axial load applied in the cross-sectional analysis was taken from the dead-load axial force of the corresponding pier in the finite element model, so that the verification remained consistent with the actual pier section used in the nonlinear analysis.

The obtained moment-curvature relationship is shown in Fig. 8, and the corresponding key performance points are summarized in Table 8. The section response exhibits a clear elastic stage, followed by a gradual yielding transition and a stable post-yield hardening branch before reaching the ultimate state. The first-yield curvature, equivalent yield curvature, and ultimate curvature were determined as 4.40×10^{-4} m^{-1}, 1.058×10^{-3} m^{-1}, and 2.896×10^{-2} m^{-1}, respectively. The corresponding bending moments were 55,409.99 kN·m, 99,491.30 kN·m, and 115,266.52 kN·m, respectively. The curvature ductility coefficient, defined as $\mu_\varphi=\varphi_u/\varphi_{ye}$, was 27.36.

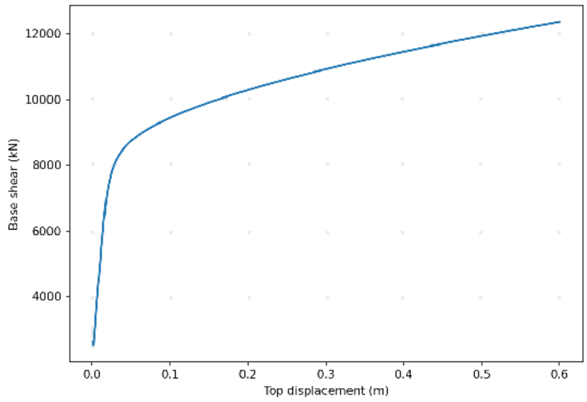

Figure 9. Pushover curve of the pier used in the finite element model

Table 9. Key performance points obtained from the pier pushover analysis

Parameter	Value
Pier height	10.0 m
Axial load	3300.59 kN
Initial stiffness	3.398×10^{8} N/m
Yield displacement	0.0291 m
Yield drift ratio	0.291%
Yield base shear	9889.38 kN
Peak base shear	12361.73 kN
Peak displacement	0.600 m

Although this verification is based on monotonic moment-curvature analysis rather than full cyclic hysteretic loading, it provides direct evidence that the fiber section adopted for the pier in the finite element model can reasonably capture the flexural yielding and nonlinear deformation capacity of the pier. Therefore, the pier model used in this study provides a more reliable basis for the subsequent nonlinear seismic response analysis and fragility assessment.

3.4 Verification of pier nonlinear static behavior

The pushover curve, expressed in terms of pier-top displacement versus base shear, is shown in Fig. 9, and the corresponding key points are summarized in Table 9. The results indicate that the pier exhibits a stable nonlinear lateral response with a clear transition from the initial elastic stage to the post-yield stage. The equivalent yield displacement and yield drift ratio were determined as 0.0291 m and 0.291%, respectively, while the corresponding base shear was 9889.38 kN. The peak base shear reached 12361.73 kN, and the displacement ductility coefficient was 20.62. These results indicate that the pier model has sufficient nonlinear deformation capacity and can reasonably represent the lateral resistance characteristics of the pier under combined axial compression and horizontal loading.

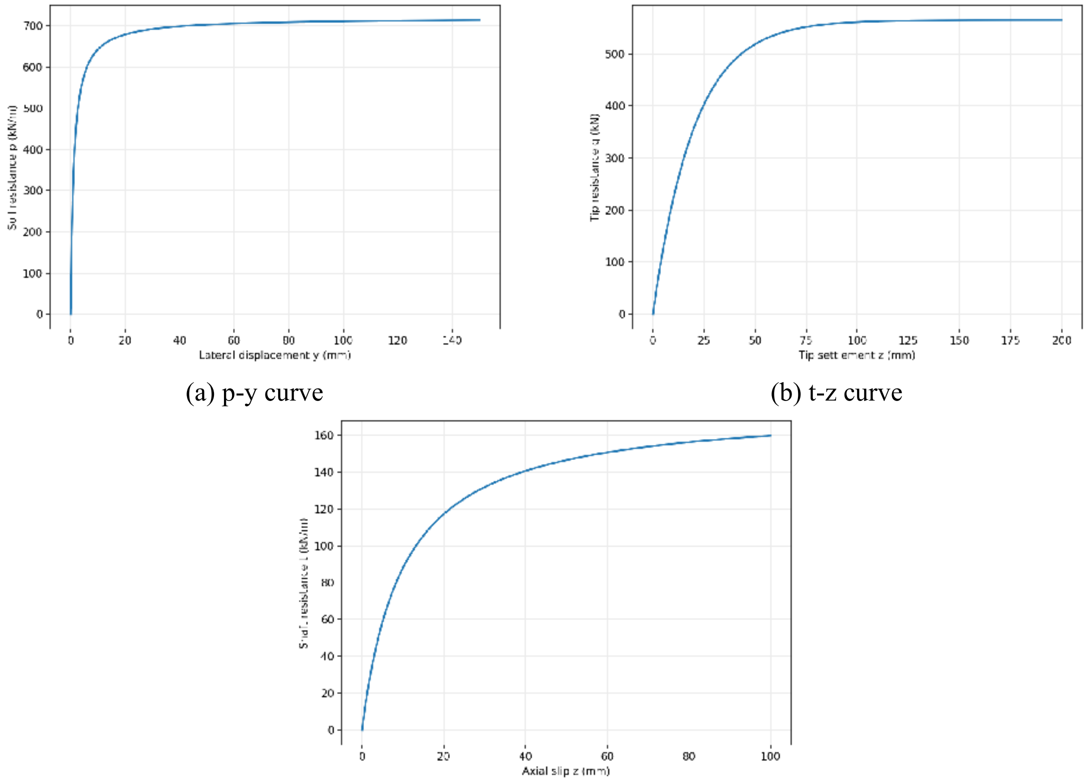

(a) p-y curve

(b) t-z curve

(c) q-z curve

Figure 10. Verified backbone curves of the adopted pile-soil spring model

Table 10. Key parameters of the verified pile-soil spring backbone relationships

Parameter	Value
Undrained shear strength, S_u	80 kPa
Initial modulus of subgrade reaction, k	60 MN/m^3
Representative pile diameter, D	1.0 m
Ultimate lateral soil resistance, p_{ult}	720.00 kN/m
Ultimate shaft friction, t_{ult}	175.93 kN/m
Ultimate end-bearing resistance, q_{ult}	565.49 kN

3.5 Verification of pile-soil spring behavior

To further support the reliability of the foundation representation adopted in this study, an independent verification of the pile-soil spring behavior was carried out based on the p-y, t-z, and q-z relationships described in Section 2.4. The verification focused on the backbone behavior of the adopted soil springs, rather than on a full bridge-level foundation analysis, so as to confirm that the selected spring parameters can reasonably represent the intended lateral soil resistance, shaft friction, and pile-tip resistance.

According to the adopted modeling parameters, the undrained shear strength was taken as Su=80 kPa and the initial modulus of subgrade reaction was taken as k=60 MN/m^3. For a representative pile diameter of 1.0 m, the ultimate lateral soil resistance of the p-y spring was calculated as p_{ult} =9.0SuD=720.00 kN/m, the ultimate shaft friction of the t-z spring was calculated as tult=0.7SuπD=175.93 kN/m, and the ultimate end-bearing resistance of the q-z spring was calculated as qult=9.0SuA=565.49 kN. The resulting p-y, t-z, and q-z backbone curves are shown in Fig. 10. The corresponding key parameters are listed in Table 10.

As shown in Fig. 10, the verified spring backbones exhibit physically reasonable nonlinear trends: the p-y curve shows an initially stiff response followed by gradual asymptotic development toward the ultimate lateral soil resistance; the t-z curve shows progressive mobilization of shaft friction with increasing axial slip; and the q-z curve shows a monotonic increase in pile-tip resistance toward the ultimate end-bearing capacity. These results confirm that the adopted pile-soil spring relationships are consistent with the parameter definitions used in this study and provide additional support for the rationality of the simplified foundation modeling under scour.

3.6 Verification of seismic response

In the dynamic time-history analysis, the classical Rayleigh damping model was employed to simulate the energy dissipation of the structure. The damping matrix [C] is expressed as a linear combination of the mass matrix [M] and the stiffness matrix [K]:[C]= α_M [M]+ β_K [K]. The coefficients α_M and β_K are determined by the specific modal circular frequencies (ω_i, ω_j) of the structure and the target damping ratio (ξ), calculated using the following formulas:

$$\alpha_M = \xi \cdot (2\omega_i\omega_j)/(\omega_i\omega_j), \tag{8}$$

$$\beta_K = \xi \cdot 2/\omega_i\omega_j. \tag{9}$$

For the reinforced concrete piers in the elastic stage, a damping ratio ξ=5% was adopted according to the Code for Seismic Design of Railway Engineering. Using the first vertical mode

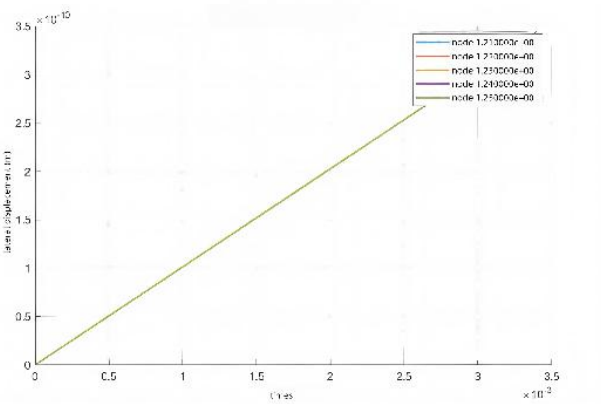

Figure 11. Structural response under seismic loading (Note: The curves represent the transverse displacement responses of different key nodes at the pier-girder connection region, with nearly coincident trends indicating the highly synchronous seismic response of each node.)

(ω_1=14.45 rad/s) and the second transverse mode (ω_2=14.83 rad/s), the calculated coefficients were α_M=0.879 and β_K=0.0027. The model was then subjected to the Northridge ground motion record, and the resulting seismic response exhibited physically realistic behavior, as illustrated in Fig. 11. Fig. 11 presents the transverse displacement time-history responses of five key nodes at the pier-girder connection regions, with the vertical axis denoting transverse displacement (in m, $\times 10^{-4}$) and the horizontal axis representing time (in s, $\times 10^{-3}$). The response curves of each node are nearly coincident with no abnormal fluctuations, which reflects the highly synchronous dynamic response of the key nodes at the pier-girder connection and verifies the good synergistic working performance between the superstructure and substructure of the bridge under seismic loading. The peak transverse displacement of the nodes reaches approximately 3.5×10^{-4} m, which is within a reasonable range and indicates that the simulated seismic response conforms to the actual mechanical characteristics of the structure.

3.7 Conclusions

The validity of the finite element model is further supported by comparisons with existing research and theoretical benchmarks. Regarding the fundamental frequencies (2.30 Hz and 2.36 Hz): Similar frequency characteristics (approximately 2.6 Hz) have been observed in the modal analysis of short-span simply supported railway bridges under moving train loads [20] and fall within the typical range reported for comparable bridges [21-23]. The maximum vertical deflection under self-weight (13.7 mm) agrees closely with the theoretical value of 14.1 mm (deviation=2.8%), confirming that the global stiffness is accurately represented.

At the component level, the independent moment-curvature and pushover analyses verify that the pier model reasonably captures the cross-sectional flexural behavior, lateral resistance, and nonlinear deformation capacity. The independently validated p-y, t-z, and q-z backbone curves further confirm that the pile-soil spring parameters provide physically reasonable behavior.

These verification results, spanning both global and component levels, confirm that the developed finite element model provides a reliable basis for the subsequent nonlinear seismic fragility analysis under scour.

4. Influence of pier material parameters on the seismic fragility of bridge components

To quantitatively assess the performance level of the bridge under seismic excitations of varying intensities, this study, based on the performance-based seismic design philosophy, classifies the damage states of the bridge system into four levels: Slight Damage, Moderate Damage, Severe Damage, and Complete Damage. The definition of each damage state focuses on quantifiable engineering responses of key components, with the specific criteria detailed in Table 11.

The damage state thresholds presented in Table 11 were selected based on established criteria from the seismic fragility literature [24], with specific consideration given to the stricter serviceability requirements of high-speed railway bridges. The pier displacement angle limits follow the performance levels defined in HAZUS-MH for reinforced concrete columns, while the bearing and sliding layer displacement limits were calibrated against Chinese railway design codes and manufacturer specifications [9]. System-level fragility is evaluated using a joint probabilistic

Table 11. Damage state criteria

Damage state	Pier damage criterion (Displacement Angle at Pier Top, θ)	Movable bearing damage criterion (Relative Displacement, Δb)	Sliding layer damage criterion (Relative Displacement, Δs)
Slight damage	$\theta \leq 0.48\%$	$\Delta b \leq 30$ mm	$\Delta s \leq 60$ mm
Moderate damage	$0.48\% < \theta \leq 1.20\%$	30 mm $< \Delta b \leq 50$ mm	60 mm $< \Delta s \leq 200$ mm
Severe damage	$1.20\% < \theta \leq 3.00\%$	50 mm $< \Delta b \leq 100$ mm	200 mm $< \Delta s \leq 300$ mm
Complete damage	$\theta > 3.00\%$	$\Delta b > 100$ mm	$\Delta s > 300$ mm

Note: The pier damage state thresholds are adopted from HAZUS-MH [24] for reinforced concrete columns. The bearing displacement thresholds follow the longitudinal design displacement grades specified for movable bearings in TB/T 1853-2018 (Steel bearings for railway bridges), Clause 3.1.2 (grades: ±30 mm, ±50 mm, ±100 mm), and are consistent with previous railway bridge seismic fragility studies [4, 5]. The sliding-layer displacement thresholds are specified with reference to the yield displacement of typical sliding-layer materials and the damage state classification framework for sliding-layer components established by Guo et al. [25] for high-speed railway simply-supported girder bridges, and are consistent with the serviceability requirements stipulated in TB 10621-2014 [9].

approach, where the system damage state is governed by the most severely damaged component, accounting for demand correlations through the covariance structure derived from IDA results. At each PGA level, the three demand parameters (θ, Δb, Δs) obtained from each ground motion record are compared against the thresholds in Table 11, and the system damage state for that record is taken as the worst state among the three components. The exceedance probability at each PGA level is then computed as the fraction of the 22 records for which the system reaches or exceeds the specified damage state. The resulting empirical probabilities are fitted with a lognormal cumulative distribution function, following the analytical fragility derivation described in Section 2.6.

4.1 Concrete strength

C35 concrete is commonly employed as the standard material in the design of current high-speed railway piers. To conduct an in-depth analysis of the influence of pier concrete strength on the seismic fragility of bridge components under scour conditions, three different concrete strength grades—C35, C40, and C45—were selected for this study. Fragility curves for both individual components and the overall system were generated separately for conditions with and without scour. This allows for a further comparison of the fragility characteristics associated with different concrete strengths.

For the sliding layer (Fig. 12), increasing concrete strength significantly lowers its damage probability. Under moderate damage (PGA=0.2 g), upgrading from C35 to C45 reduces the probability by 10.9% (no scour) and 10.0% (scour). Scour itself reduces the sliding layer's fragility compared to the non-scour case; for C35 at PGA=0.4 g (severe damage), the probability is 22.8% lower under scour.

For movable bearings (Fig. 13), the benefit of higher concrete strength is more pronounced, especially without scour. Under severe damage (PGA=0.4 g), upgrading from C35 to C45 decreases probability by 15.2% (no scour) and 6.2% (scour). Scour consistently increases bearing fragility across all concrete grades.

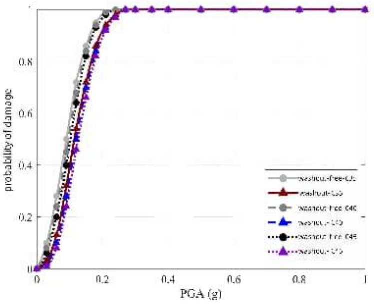

(a) Slight damage

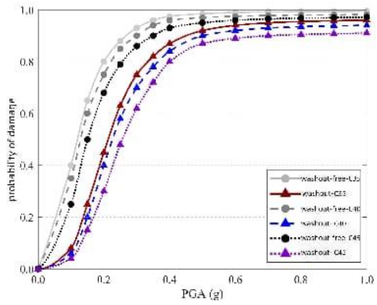

(b) Moderate damage

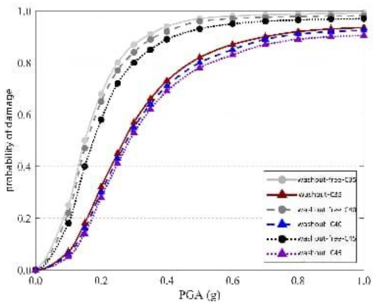

(c) Severe damage

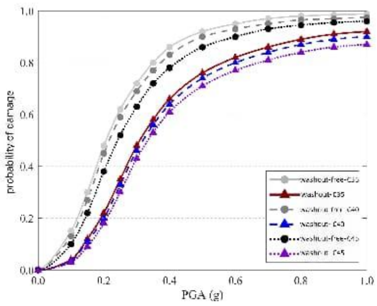

(d) Complete damage

Figure 12. Influence of pier concrete strength on the seismic fragility of the sliding layer under scour effects

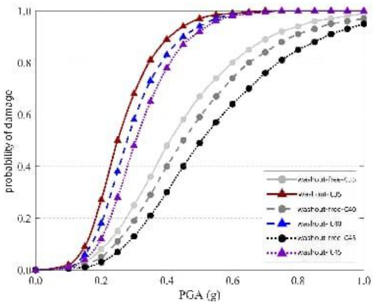

(a) Slight damage

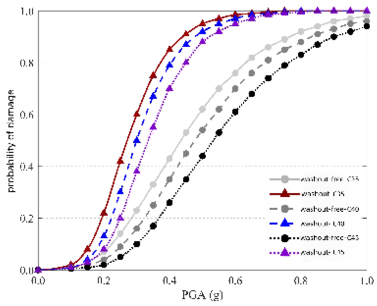

(b) Moderate damage

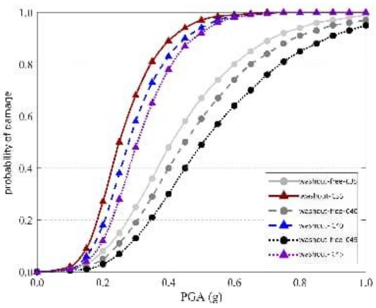

(c) Severe damage

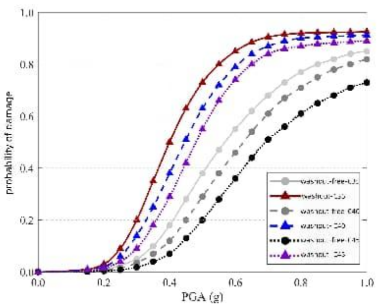

(d) Complete damage

Figure 13. Influence of pier concrete strength on the seismic fragility of movable bearings under scour effects

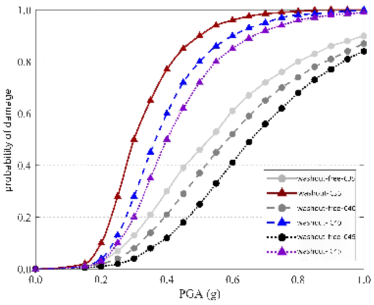

(a) Slight damage

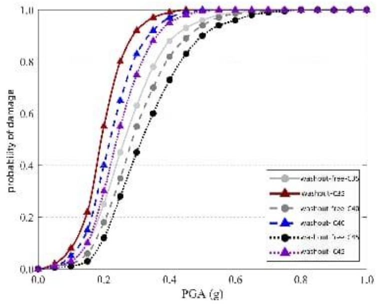

(b) Moderate damage

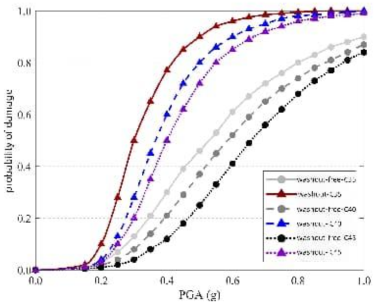

(c) Severe damage

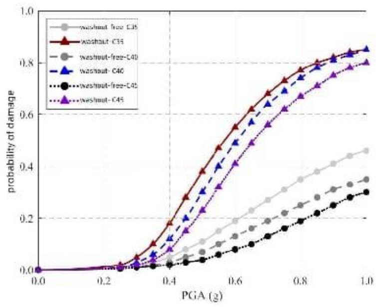

(d) Complete damage

Figure 14. Influence of pier concrete strength on the seismic fragility of the pier under scour effects

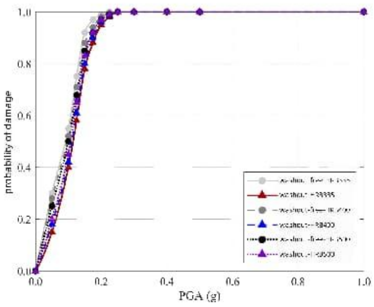

(a) Slight damage

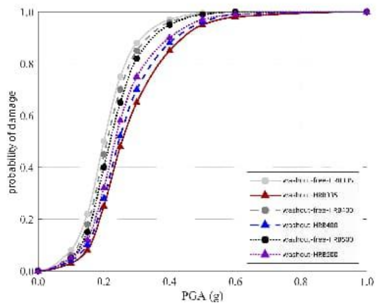

(b) Moderate damage

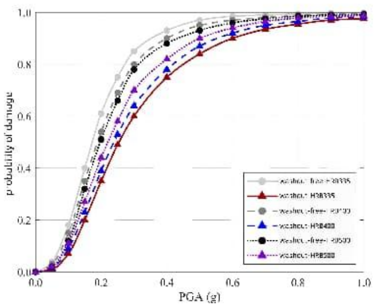

(c) Severe damage

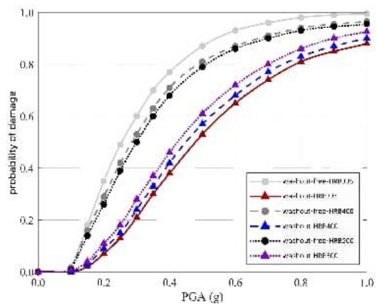

(d) Complete damage

Figure 15. Influence of pier longitudinal reinforcement strength on the seismic fragility of the sliding layer under scour effects

The most significant effect is observed for the pier itself (Fig. 14). Under severe damage (PGA=0.4 g), increasing concrete strength from C35 to C45 reduces the pier's damage probability by approximately 25.5%. However, scour substantially elevates the pier's fragility, underscoring its vulnerability when foundation support is degraded.

The apparent reduction in sliding layer fragility under scour is attributed to period elongation (0.424 s→0.487 s), which reduces spectral acceleration for the selected ground motion suite. At PGA=0.4 g, median sliding layer displacement decreases from 58 mm (non-scoured) to 45 mm (scoured), consistent with the fragility shift. However, this is a spectrum-dependent phenomenon and does not indicate an overall benefit of scour—while scour increases absolute fragility across all components, the relative mitigating effect of stronger concrete remains valid, particularly for the sliding layer and pier. In summary, enhancing concrete strength is an effective strategy for lowering system fragility, with the most substantial gains observed for the pier component.

4.2 Longitudinal reinforcement strength

This section analyzes the impact of longitudinal reinforcement grade (HRB335, HRB400, HRB500) on seismic fragility. A consistent hierarchy is observed across all components: HRB335 exhibits the highest fragility, followed by HRB400, with HRB500 being the most effective in reducing damage probability. The detrimental effect of scour is universal but interacts differently with reinforcement strength for each component.

For the sliding layer (Fig. 15), higher reinforcement strength lowers its fragility. Under severe

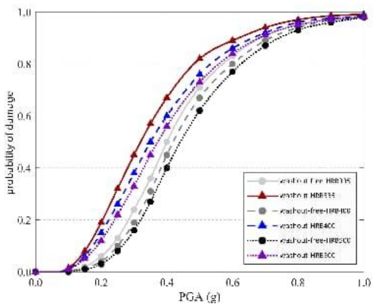

(a) Slight damage

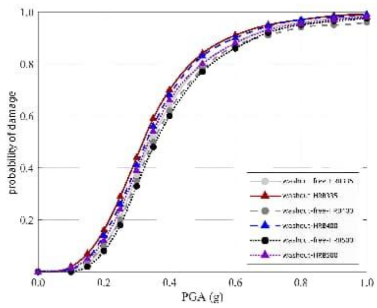

(b) Moderate damage

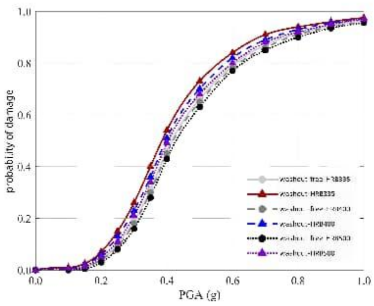

(c) Severe damage

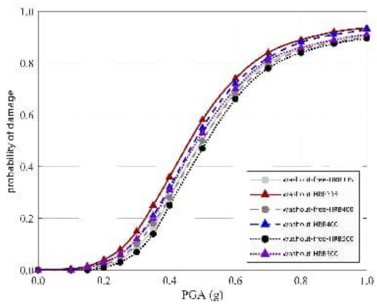

(d) Complete damage

Figure 16. Influence of pier longitudinal reinforcement strength on the seismic fragility of movable bearings under scour effects

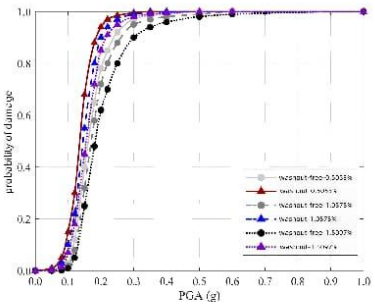

(a) Slight damage

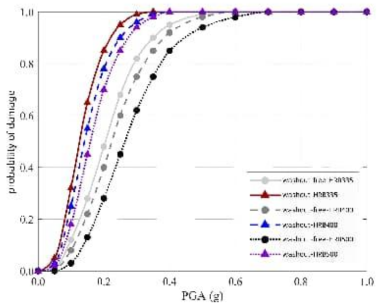

(b) Moderate damage

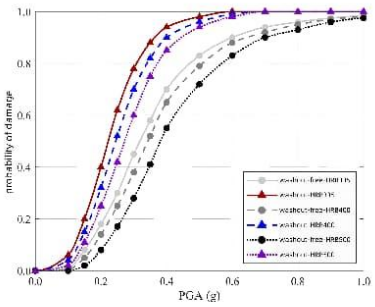

(c) Severe damage

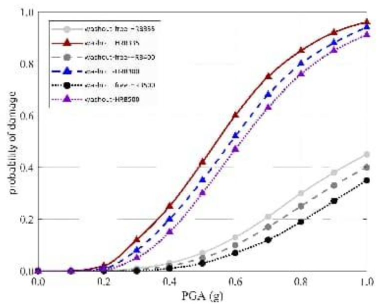

(d) Complete damage

Figure 17. Influence of pier longitudinal reinforcement strength on the seismic fragility of the pier itself under scour effects

damage (PGA=0.4 g), the damage probability for non-scour conditions decreases from approximately 92% (HRB335) to 87% (HRB500). The beneficial effect of higher-strength reinforcement is attenuated under scour, indicating that scour adversely impacts the sliding layer's seismic capacity independently of reinforcement grade.

The seismic performance of movable bearings (Fig. 16) is significantly enhanced by using higher-strength reinforcement. Under identical scour conditions, HRB500 bearings show the lowest fragility. Scour substantially increases the fragility of bearings across all reinforcement grades, though this effect diminishes at very high PGA levels (>0.8 g). Upgrading reinforcement strength can partially mitigate the scour-induced increase in fragility, especially in the moderate damage stage.

The reinforcement grade exerts the most pronounced influence on the pier itself (Fig. 17). The fragility hierarchy (HRB500<HRB400<HRB335) is clear across all damage states. Scour drastically increases the pier's fragility, particularly in the low to moderate PGA range (0.1-0.3 g), where damage probability can be 100-200% higher under scour for HRB335. While the influence of scour gradually decreases with increasing PGA, it remains significant.

In summary, upgrading longitudinal reinforcement strength is an effective measure for improving seismic performance, with the most critical impact on the pier. However, scour profoundly increases component fragility, and its effect partially offsets the benefits of stronger reinforcement for the sliding layer and bearings, underscoring the necessity of combining material improvement with scour protection.

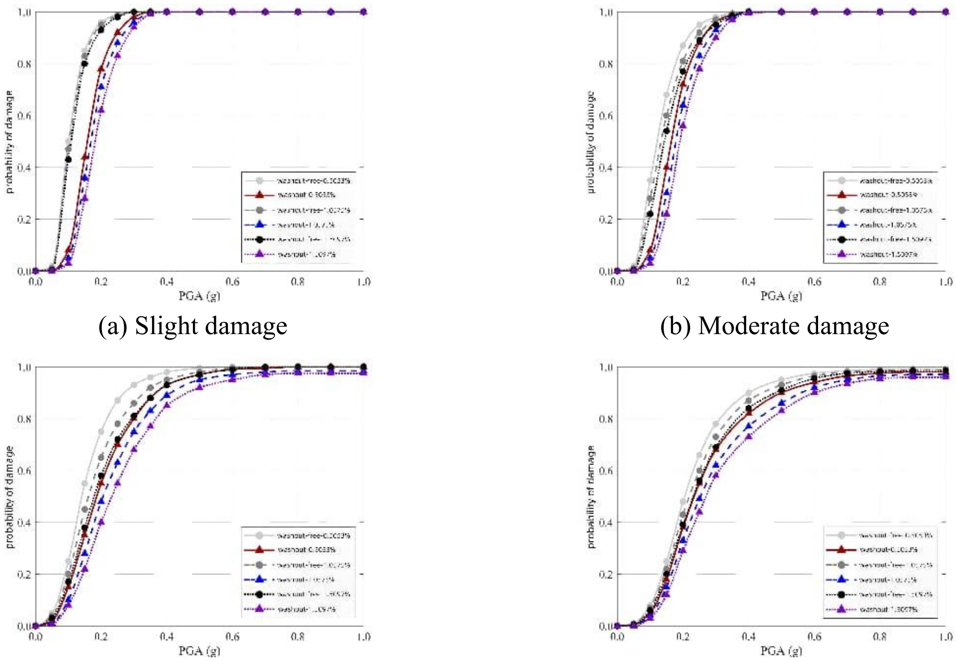

(a) Slight damage (b) Moderate damage

(c) Severe damage (d) Complete damage

Figure 18. Influence of pier reinforcement ratio on the seismic fragility of the sliding layer under scour effects

4.3 Reinforcement ratio

This section investigates the influence of the pier reinforcement ratio (0.5053%, 1.0575%, 1.5097%) on system seismic fragility. The results demonstrate that the reinforcement ratio is the most influential material parameter considered, with a higher ratio consistently yielding the lowest fragility across all components. The effect of scour, however, varies significantly depending on the component.

For the sliding layer (Fig. 18), increasing the reinforcement ratio substantially improves its seismic performance. Under slight damage (PGA=0.1 g, no scour), increasing the ratio from 0.5053% to 1.5097% reduces the damage probability by about 17.6%. This benefit diminishes at high PGA levels (>0.3 g). Contrary to its effect on other components, scour appears to slightly reduce the sliding layer's fragility (curves shift right), likely by altering the global dynamic response and reducing force transmission.

The fragility of movable bearings (Fig. 19) is highly sensitive to the pier reinforcement ratio. Under moderate damage (PGA=0.4 g), increasing the ratio from the minimum to the maximum value can reduce the bearing damage probability by approximately 50%. Scour exerts a strong adverse effect on bearings, significantly increasing their fragility—for example, by 60% for the lowest reinforcement ratio at PGA=0.5 g (moderate damage). This is attributed to scour-induced changes in pier stiffness and dynamic characteristics.

The pier's own fragility (Fig. 20) is most effectively controlled by its reinforcement ratio. A clear trend shows lower fragility with a higher ratio. Scour markedly increases pier fragility across

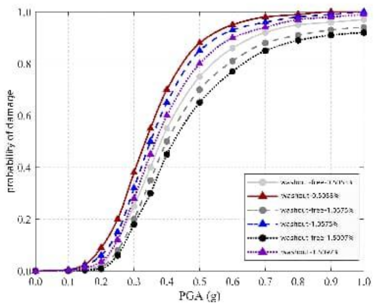

(a) Slight damage

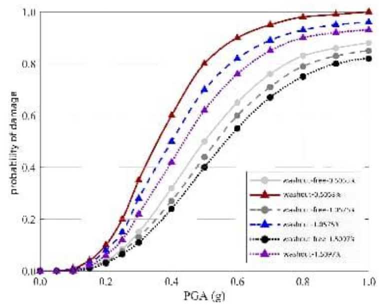

(b) Moderate damage

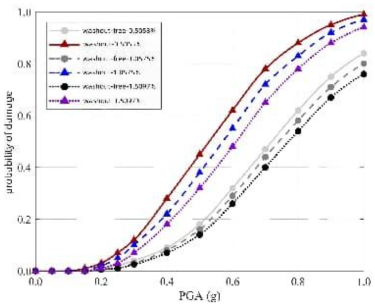

(c) Severe damage

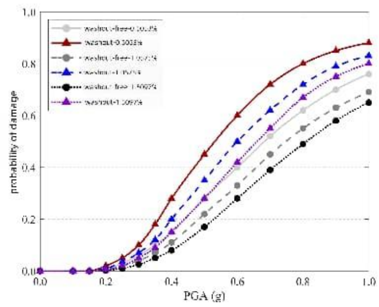

(d) Complete damage

Figure 19. Influence of pier reinforcement ratio on the seismic fragility of movable bearings under scour effects

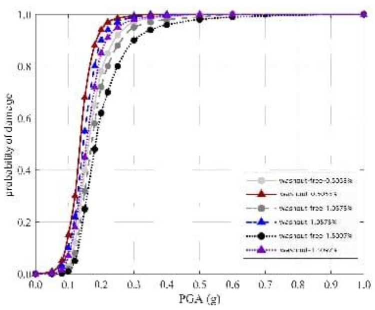

(a) Slight damage

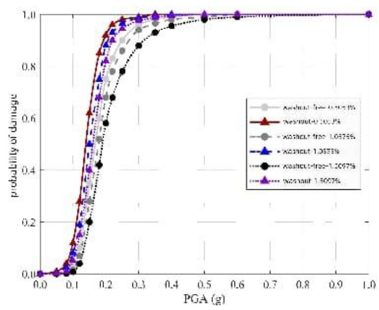

(b) Moderate damage

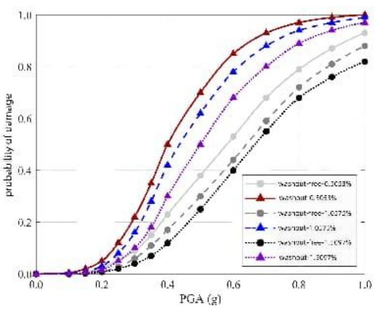

(c) Severe damage

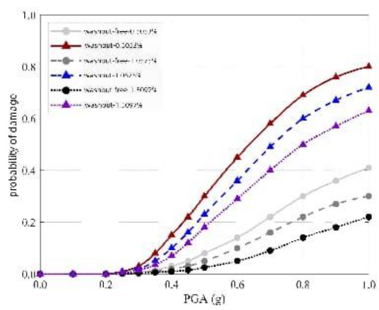

(d) Complete damage

Figure 20. Influence of pier reinforcement ratio on the seismic fragility of the pier itself under scour effects

all ratios, but a high reinforcement ratio provides notable resilience. At a PGA of 0.2 g, the damage probability for the highest ratio is 0.60, compared to 0.85 for the lowest—a reduction of 29%. The detrimental impact of scour is more severe for piers with a low reinforcement ratio.

In summary, optimizing the pier reinforcement ratio is the most effective single measure for enhancing the seismic resilience of the entire bridge system. While a higher ratio significantly mitigates pier fragility and protects bearings, the component-specific role of scour must be acknowledged: it adversely affects piers and bearings but may inadvertently slightly benefit the sliding layer through system detuning. This confirms the reinforcement ratio as the paramount parameter for performance-based design under combined seismic and scour hazards.

5. Analysis of parameter interactions

5.1 Synergistic effect index

To quantitatively evaluate the interaction between different material parameter enhancements, a Synergistic Effect Index (SEI) is proposed [26]. It is defined as the ratio of the damage probability reduction achieved by a combined parameter optimization to the sum of the reductions achieved by optimizing each parameter individually:

$$SEI = \frac{P_{bench}-P_{comb}}{(P_{bench}-P_A)+(P_{bench}-P_B)}, \tag{10}$$

where P_{bench} is the damage probability of the benchmark configuration (e.g., C35 concrete, HRB335 reinforcement, reinforcement ratio 0.5053%) at the specified intensity level and damage state; P_A is the damage probability of the configuration with only Parameter A enhanced (e.g., concrete strength upgraded to C45), while all other parameters remain at benchmark values; P_B is the damage probability of the configuration with only Parameter B enhanced (e.g., reinforcement strength upgraded to HRB500); P_{comb} is the damage probability of the configuration with both Parameters A and B enhanced simultaneously.

The physical meaning of the Synergistic Effect Index is as follows:

SEI>1 Synergistic effect. The combined reduction in damage probability is greater than the sum of individual reductions, indicating positive interaction between the two parameters.

SEI=1: Additive effect. The combined reduction equals the sum of individual reductions, implying no interaction.

SEI<1: Antagonistic effect. The combined reduction is less than the sum of individual reductions, indicating diminishing marginal returns or negative interaction.

Statistical interpretation: The SEI is a deterministic metric derived from fragility probabilities at a specific intensity level. It does not represent a statistical estimate with confidence bounds but rather a comparative measure of effectiveness. The index is most meaningful when evaluated at intensity levels corresponding to significant damage probabilities (e.g., PGA=0.4 g, where damage probabilities for the benchmark configuration are in the range of 0.6-0.9), as the interaction effects are most pronounced under moderate-to-high nonlinear response.

Applicability: The SEI is defined for pairwise comparisons of material parameters and is specific to the considered damage state and intensity level. In this study, the index is evaluated for severe damage at PGA=0.4 g under scoured conditions, as this represents the most critical scenario for bridge performance. Extrapolation of the index to other damage states or intensity

Table 12. Damage probability and interaction analysis under PGA=0.4g with scour

Optimization scenario	Damage probability	Reduction (Δ)	Synergistic effect index
Benchmark (C35, HRB335, 0.5053%)	0.900	-	-
Concrete→C45	0.645	0.255	-
Reinforcement→HRB500	0.800	0.100	-
Reinforcement ratio→1.5097%	0.765	0.135	-
Concrete (C45)×Reinforcement (HRB500)	0.600	0.300	0.85
Concrete (C45)×Reinforcement Ratio (1.5097%)	0.580	0.320	0.82
Reinforcement (HRB500)×Ratio (1.5097%)	0.700	0.200	0.85

levels should be avoided without re-evaluation, as the nature of parameter interactions may vary with the extent of structural nonlinearity.

5.2 Calculation results and summary

The damage probabilities for individual and combined parameter enhancements are summarized in Table 12. The corresponding reductions and calculated Synergistic Effect Indices are also presented.

The calculated Synergistic Effect Indices for all three pairwise combinations are less than 1.0 (0.85, 0.82, and 0.85), clearly demonstrating an antagonistic effect. This indicates that under the combined action of high-intensity seismic shaking (PGA=0.4 g) and scour (6 m depth), the marginal benefit of simultaneously optimizing two material parameters diminishes. The physical explanation lies in the shift of failure mode under deep nonlinearity: once the pier enters significant inelastic deformation, further material enhancements—particularly those affecting flexural capacity—may not yield proportional reductions in damage probability, as the response becomes increasingly governed by global stability and soil-structure interaction rather than local material strength. This finding underscores the importance of prioritizing the most influential parameter (reinforcement ratio) before considering additional upgrades, as suggested in the design recommendations (Section 6.2).

5.3 Sensitivity analysis of material parameters

To quantitatively evaluate the relative importance of each material parameter on system vulnerability, a sensitivity index was used for quantitative sensitivity analysis. The sensitivity index (SI) of parameter P is defined as the relative change in damage probability at PGA=0.4 g when the parameter changes from its minimum value to its maximum value:

$$SI_P = \frac{P_{\text{damage}}(P_{max}) - P_{\text{damage}}(P_{min})}{P_{\text{damage}}(P_{min})}. \tag{11}$$

Table 13 presents the sensitivity indices for the three material parameters under both non-scoured and scoured conditions.

The results demonstrate that the reinforcement ratio exhibits the highest sensitivity index under both conditions (-0.25 and -0.22), confirming its dominant role in controlling system fragility.

Table 13. Sensitivity indices of material parameters (at PGA=0.4 g, severe damage state)

Parameter	Variation range	Non-scoured	Scoured (6 m)
Concrete strength	C35→C45	-0.18	--0.15
Reinforcement strength	HRB335→HRB500	-0.11	--0.08
Reinforcement ratio	0.5053%→1.5097%	-0.25	-0.22-

Concrete strength shows moderate sensitivity, while reinforcement strength alone has the least influence. Under scoured conditions, all sensitivity indices decrease slightly, indicating that scour attenuates the effectiveness of material upgrades—consistent with the antagonistic effect discussed in Section 5.2.

6. Conclusions

6.1 Key conclusions

(1) The longitudinal reinforcement ratio is identified as the most influential parameter for controlling system-level seismic fragility. Increasing the reinforcement ratio from 0.5053% to 1.5097% reduces the probability of severe damage at PGA=0.4 g by approximately 25% under non-scoured conditions and 22% under scoured conditions, outperforming improvements in concrete strength or reinforcement grade alone.

(2) Scour consistently increases the seismic fragility of all bridge components, with the most pronounced effect observed on piers and movable bearings. Under scour depth of 6 m, the median seismic capacity for severe damage decreases by 16-18% across all material configurations. However, the apparent reduction in sliding layer fragility under scour is attributed to period elongation (0.424 s→0.487 s) and is spectrum-dependent, not an overall benefit of scour.

(3) An antagonistic effect exists when multiple material parameters are simultaneously upgraded under combined high-intensity shaking (PGA=0.4 g) and scour. The Synergistic Effect Index values for all pairwise combinations range from 0.82 to 0.85, indicating that the combined benefit is less than the sum of individual improvements. This reflects diminishing marginal returns under deep nonlinear response.

(4) The probabilistic seismic demand models developed for each component exhibit strong correlations (R^2=0.86-0.92) between PGA and engineering demand parameters, validating the chosen intensity measure. The dispersion parameters (βEDP|IM=0.35-0.45) quantify the record-to-record variability, providing a statistical basis for the fragility estimates. Sensitivity analysis confirms the reinforcement ratio as the most influential parameter, with a sensitivity index of -0.25 under non-scoured conditions, followed by concrete strength (-0.18) and reinforcement strength (-0.11).

6.2 Research practical value

6.2.1 Applicability of findings

The findings of this study are directly applicable to High-speed railway simply-supported girder bridges of similar configuration (32 m span, round-ended solid piers, pile foundation) in seismic regions with scour potential. Material selection and optimization within the ranges investigated (C35-C45 concrete, HRB335-HRB500 reinforcement, 0.5053%-1.5097% reinforcement ratio). Performance-based design and assessment frameworks that require quantitative relationships between material parameters and system fragility. Retrofitting prioritization for existing bridges, where reinforcement ratio enhancement can be targeted as the most effective intervention. The observed trends—particularly the dominance of reinforcement ratio and the antagonistic effect—are expected to hold for similar bridge types with comparable dynamic characteristics. However, the absolute fragility values are specific to the bridge configuration, soil conditions, and ground motion suite employed in this study.

6.2.2 Limitations and future work

(1) Parameter range: While three levels were investigated for each material parameter, the full continuum of possible values was not explored. Future studies should expand the range to include additional grades (e.g., C50 concrete, HRB600 reinforcement) and intermediate reinforcement ratios.

Scour representation: Scour was idealized as a fixed depth of 6 m, corresponding to the general scour depth under the design flood estimated per JTS 167-4-2012, with uniform removal of soil springs. In reality, scour depth varies with hydrological conditions, evolves over time, and may create complex scour holes. Time-varying scour processes and probabilistic scour depth distributions should be considered in future research.

(2) Ground motion suite: Although 22 spectrally matched records were employed, a larger set would further enhance statistical robustness. The spectrum-dependent nature of certain observations (e.g., sliding layer response) underscores the need for caution in generalizing to sites with different seismic hazard characteristics.

Experimental validation: The numerical model was validated against global response characteristics (frequencies, displacements) and theoretical benchmarks. Component-level experimental validation under cyclic loading would further strengthen confidence in the absolute fragility estimates.

(3) Emerging materials: This study focused on conventional materials prescribed by current Chinese railway codes. Future research should explore the applicability of sustainable materials (e.g., fiber-reinforced recycled aggregate concrete, carbonated cementitious composites) in railway bridge applications, particularly regarding their cyclic performance and long-term durability.

(4) Addressing these limitations represents promising directions for advancing the multi-hazard fragility assessment of bridges in scour-prone seismic regions.

6.3 Engineering design optimization

Based on the quantitative findings of this study, a three-tiered design strategy is proposed for high-speed railway bridges in scour-prone seismic regions. Each recommendation is directly supported by the analysis results presented in Sections 4 and 5.

(1) Optimize the reinforcement ratio as the primary measure. The results in Section 4.3 demonstrate that increasing the reinforcement ratio from 0.5053% to 1.5097% reduces the probability of severe damage at PGA=0.4 g by approximately 25% under non-scoured conditions and 22% under scoured conditions—a more significant reduction than achieved by upgrading concrete strength (18% under non-scoured, 15% under scoured) or reinforcement grade (11% under non-scoured, 8% under scoured) alone. Therefore, designs should prioritize achieving a

reinforcement ratio in the range of 1.0%-1.3% before considering other material upgrades. This range is proposed as it balances the significant fragility reduction observed at 1.5097% with practical constructability and economic considerations.

(2) Select material grades rationally after achieving optimal reinforcement ratio. The antagonistic effect quantified in Section 5 (SEI=0.82-0.85) demonstrates that simultaneously maximizing multiple material properties yields diminishing returns under extreme conditions. After setting an optimal reinforcement ratio, a balanced upgrade of material grades (e.g., to C40 concrete and HRB400/500 reinforcement) is recommended. This enhances capacity while avoiding the diminished returns observed from simultaneous maximization. The selection should be guided by site-specific seismic hazard levels: for high-hazard sites, upgrading to C45 and HRB500 may still be warranted despite the antagonistic effect.

(3) Integrate Scour Protection as a Mandatory Design Condition. The degrading effect of scour cannot be fully compensated by material design alone, highlighting the critical role of integrated monitoring [27] and physical countermeasures like riprap protection. Site-specific scour assessment and protective measures (e.g., riverbed armoring [28]) must be mandated. The design analysis should explicitly consider the target lifetime scour depth.

These design recommendations carry important implications for engineering practice. First, the identification of reinforcement ratio as the most influential parameter provides a clear basis for prioritizing retrofitting interventions on existing bridges: when resources are limited, efforts should focus on increasing the reinforcement ratio of piers rather than indiscriminately upgrading material grades across all components. Second, the observed antagonistic effect under combined high-intensity shaking and scour informs performance-based assessment frameworks—engineers should recognize that the marginal benefit of simultaneous material upgrades diminishes under extreme conditions, and design verification should account for this nonlinearity. Third, the consistent fragility increase due to scour across all material parameters emphasizes that site-specific scour assessment must be integrated into seismic design workflows; neglecting scour in fragility analyses may lead to non-conservative damage probability estimates, particularly for bridges in riverine environments. Collectively, these implications bridge the gap between the quantitative findings of this study and their practical application in the design, assessment, and retrofitting of railway bridges facing combined seismic and scour hazards.

References

1. Wang, M., Shen, Z.K. (2020). Present-day crustal deformation of continental China derived from GPS and its tectonic implications. Journal of Geophysical Research: Solid Earth, 125(2), e2019JB018774. https://doi.org/10.1029/2019JB018774.
2. Pang, Y., Luo, Q., Wei, K., Deng, K., Chen, X. (2025). Seismic resilience assessment of reinforced concrete bridges constructed with tall piers in the deep-water environment. Engineering Structures, 325, 119387. https://doi.org/10.1016/j.engstruct.2025.119387.
3. Ren, W.J., Qiu, D.P., Zhang, Z., Liu, C.G. (2024). Two-dimensional seismic fragility analysis of offshore bridges considering seismic correlation of components. Technology for Earthquake Disaster Prevention, 19(1), 96-107. https://doi.org/10.11899/zzfy20240110.
4. Hu, D.Y. (2021). Seismic fragility analysis of typical continuous girder bridges on Yukun High-Speed Railway. Journal of Railway Science and Engineering, 18(2), 297-305.
5. Qu, F.X., Han, L.L., Deng, X.D. (2021). Seismic retrofit scheme for existing simply supported girder bridges based on seismic fragility. Sichuan Architecture, 4(6), 171-172, 174.

6. Sun, Q. (2024). Time-varying seismic resilience analysis of RC bridge piers under scour action. Hunan Communication Science and Technology, 50(2), 45-49.
7. Antonopoulos, C., Tubaldi, E., Carbonari, S., Gara, F., Dezi, F. (2025). Dynamic behaviour and seismic response of scoured bridge piers. Infrastructures, 10(4), 75. https://doi.org/10.3390/infrastructures10040075.
8. Nettis, A., Nettis, A., Ruggieri, S., Uva, G. (2024). Corrosion-induced fragility of existing prestressed concrete girder bridges under traffic loads. Engineering Structures, 314, 118302. https://doi.org/10.1016/j.engstruct.2024.118302.
9. National Railway Administration of China (2014). Code for design of high speed railway (TB 10621-2014). China Railway Publishing House, Beijing, China.
10. Mander, J.B., Priestley, M.J.N., Park, R. (1988). Theoretical stress-strain model for confined concrete. Journal of Structural Engineering, 114(8), 1804-1826. https://doi.org/10.1061/(ASCE)0733-9445(1988)114:8(1804).
11. Ariza, G. C. F., Perraud, Y., Chatzigogos, C. (2023). Influence of Rayleigh waves on seismic fragility curves for reinforced concrete bridge pylons. HAL Open Science, hal-04123456.
12. Phatsak, S., Kongkitkul, W. (2025). Effects of bidirectional lateral loading on the bearing capacity and p-y behavior of single piles. GEOMATE Journal, 28(125), 10-17.
13. Zaidan, J., Bennabi, A., Poupardin, A., Benamar, A., Marin, F. (2024). Spatio-temporal characterisation of local scour around a circular bridge pier in cohesive soil with different clay/silt ratio. European Journal of Environmental and Civil Engineering, 28(14), 3328-3347. https://doi.org/10.1080/19648189.2024.2338784.
14. Vuong, T.H.N., Wu, T.R., Huang, Y.X., Chu, C.R., Wang, C.Y., Le, T.L. (2024). Numerical study of local scour and hydrodynamic pressure of complex bridge piers. Results in Engineering, 24, 103533. https://doi.org/10.1016/j.rineng.2024.103533.
15. American Petroleum Institute (2000). Recommended practice for planning, designing and constructing fixed offshore platforms—working stress design (API RP 2A-WSD) (21st Edition). American Petroleum Institute, Washington, D.C., USA.
16. Ministry of Transport of the People’s Republic of China (2012). Code for pile foundation of port engineering (JTS 167-4-2012). People’s Communications Press, Beijing, China.
17. Cornell, C.A., Jalayer, F., Hamburger, R.O., Foutch, D.A. (2002). Probabilistic basis for 2000 SAC federal emergency management agency steel moment frame guidelines. Journal of Structural Engineering, 128(4), 526-533. https://doi.org/10.1061/(ASCE)0733-9445(2002)128:4(526).
18. Baker, J.W. (2015). Efficient analytical fragility function fitting using dynamic structural analysis. Earthquake Spectra, 31(1), 579-599. https://doi.org/10.1193/021113EQS025M.
19. Mackie, K.R., Stojadinović, B. (2005). Fragility basis for California highway overpass bridge seismic decision making. PEER Report 2005/02; Pacific Earthquake Engineering Research Center, Berkeley, CA, USA.
20. Rahman, A.K., Imam, B., Hajializadeh, D. (2024). A simplified method for estimating bridge frequency effects considering train mass. Frontiers in Built Environment, 10, 1382210. https://doi.org/10.3389/fbuil.2024.1382210.
21. Li, X., Zhang, D. (2021). Finite element modeling and modal analysis of steel truss railway bridges. Journal of the China Railway Society, 43(6), 117-126.
22. Wang, S., Li, H., Chen, G. (2020). Vibration characteristics and train-induced response of long-span steel truss railway bridges. Journal of Railway Engineering Society, 37(4), 67-75.
23. FEMA (2003). HAZUS-MH: Multi-hazard loss estimation methodology, earthquake model, advanced engineering building module. Federal Emergency Management Agency, Washington, D.C., USA.
24. Guo, W., Li, Y.S., Hu, Y., Xu, Z.A. (2016). Failure analysis on multi-span simply-supported girder bridge of high-speed railway under strong earthquakes. New technologies, progress and applications in engineering earthquake prevention and disaster reduction. Hefei University of Technology Press, Hefei, China.
25. Decò, A., Frangopol, D.M. (2011). Risk assessment of highway bridges under multiple hazards. Journal

of Risk Research, 14(9), 1057-1089. https://doi.org/10.1080/13669877.2011.571789.
26. Prendergast, L.J., Gavin, K. (2014). A review of bridge scour monitoring techniques. Journal of Rock Mechanics and Geotechnical Engineering, 6(2), 138-149. https://doi.org/10.1016/j.jrmge.2014.01.007.
27. Lauchlan, C.S., Melville, B.W. (2001). Riprap protection at bridge piers. Journal of Hydraulic Engineering, 127(5), 412-418. https://doi.org/10.1061/(ASCE)0733-9429(2001)127:5(412).